

# Experimental study of the wake past cubic wall-mounted elements to predict flow variations for tidal turbines.

Maria Ikhennicheu\*, Grégory Germain\*, Benoît Gaurier\* Philippe Druault†

\*Marine Structure Laboratory, IFREMER, 150 Quai Gambetta, 62200 Boulogne sur Mer. France

E-mail: gregory.germain@ifremer.fr

†Sorbonne Universités, UPMC Univ Paris 06, CNRS, UMR 7190, Institut Jean Le Rond d'Alembert, F-75005 Paris, France

E-mail: philippe.druault@upmc.fr

**Abstract**—There is a strong tidal energy potential in France, especially in the Alderney Race. In the area of study, where turbines will be installed, bathymetry variations are causing velocity fluctuations with a high turbulence rate in the water column: large coherent turbulent structures can be observed at the sea surface. Such events can have a major impact on the marine tidal turbines behaviour and structural fatigue.

To reproduce and analyse these turbulent events, tests are carried out in the wave and current circulating flume tank of IFREMER in Boulogne-sur-Mer. Before trying to reproduce a complex bathymetry, we chose to introduce the topic by studying elementary obstacles representative of real seabed elements (with an aspect ratio of the magnitude of the mean bathymetry variations): a wide square cylinder and an inclined floor. Experiments are carried out with Reynolds number as high as achievable in Froude similitude:  $Re = 2.5 \times 10^5$  and  $F_r = 0.23$ .

The impact of the aspect ratio is studied by comparing results obtained with PIV and LDV measurements on the cube and cylinder cases. The addition of an inclined floor is also investigated. Results show a significant increase of the wake with the aspect ratio. The inclined floor induces a reduction of the shear layer created by the obstacle and modifications on the shedding frequency.

**Index Terms**—Turbulence, Experimental trials, wall-mounted obstacles, LDV, PIV

## I. INTRODUCTION

The idea of harvesting energy from the sea dates back to antiquity, however it is only recently that industrial projects have started to emerge. There is a strong tidal potential in France: over 20% of the European potential is located in French water, especially in the Alderney Race (*Raz-Blanchard*) that presents currents up to  $U_{insitu} = 5m/s$ . Surveys performed in this area give access to the bathymetry (see fig. 1) showing an average depth variation of  $H_{insitu} = 5m$ . The Reynolds number *in situ*, based on  $H_{insitu}$  and  $U_{insitu}$  and the kinematic viscosity of water  $\nu$ , is high:  $Re_{insitu} = H_{insitu}U_{insitu}/\nu = 2.5 \times 10^7$  and strong velocity variations exist. Such variations are causing a high turbulence rate in the water column, where marine current turbines are meant to be installed. Turbulence can have a major impact on the tidal turbines, on their production [1] and on the structural fatigue [2]. Before trying to reproduce complex structures, we chose to introduce the topic by

studying elementary obstacles representative of real life condition: *i.e.* with an aspect ratio of the magnitude of the mean bathymetry variations encountered between France and Alderney.

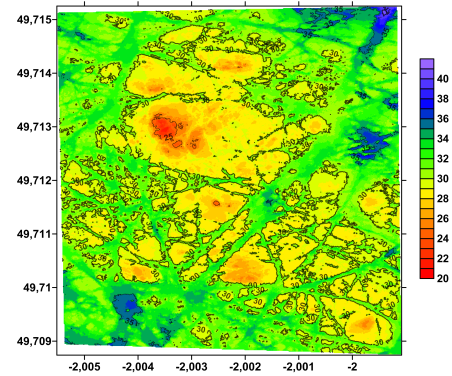


Fig. 1: Bathymetry of the the Alderney Race (between Cherbourg and Alderney) in the studied area.

The wall-mounted cube is a widely studied obstacle in the literature and this case was developed in [3,4]. The impact of the aspect ratio ( $A_R = \text{Width/Height}$ ), although fundamental (see [5]) is not often investigated in the literature. One of the most extensive study on the topic is the experimental work of Lee et al. [6], at  $Re = 5 \times 10^4$ . They studied the influence of  $A_R$  but only with factors of 0.5, 1, and 2. More extensive studies on  $A_R$  and its impact on the wake are even less common.  $A_R$  was experimentally studied in the work of Martinuzzi & Troppea [7]. They found that for  $A_R > 6$ , the recirculation region downstream of the cube switches from a 3D aspect to a nominally 2D aspect. Another experimental study of  $A_R$  was achieved at low  $Re$  [8], showing global wake behaviour for various  $A_R$ . For obstacles with high  $A_R$ , the two ends of the horseshoe vortex are farther apart and have smaller influence on the middle region of the wake, unlike for small  $A_R$  obstacles where they interact and cause a very 3D behaviour of the wake. Martinuzzi & Troppea [7] show the evolution of the recirculation end downstream of

the obstacle from a clear point for a 3D cube to an array of alternating saddle and node points similar to rib ( $A_R = \infty$ ) cases when  $A_R > 10$ . The main differences between 2D and 3D square obstacles are described by Schofield & Logan [5] in matter of recovery rate and recirculation length that significantly increase for ribs.

The case of  $A_R = \infty$  is a classical example of a 2D<sup>1</sup> obstacle in the literature. Among the first to ever characterize the flow past a 2D block (= rib), Castro [9] characterized its wake at  $Re = 1.5 \times 10^4$ . He underlines the effect of the boundary layer height  $\delta^*$ , especially on the reattachment of the flow on the top surface of a square rib that occurs if  $\delta^* \gg 1$ . More recently, Liu et al. [10] carried out experiments on a rib in a turbulent flow for  $Re = 1.3 \times 10^4$  and  $\delta^* < 1$ . They give a detailed explanation of the intermittency aspect of the reattachment of the recirculation region and found that the reattachment position  $x_{ds}^* = x_{ds}/H$  is  $x_{ds}^* = 9.75$ . The value is similar in [11]:  $x_{ds}^* \sim 11.5$ . Liu et al. [10] also found that for  $x^* = 15.75$  the streamwise velocity is not fully recovered, whereas it is in the wake of the 3D wall-mounted cube (see [12]). Finally, the experimental works of Wang et al. [13] offer a topology of the fluid past a rib at  $Re = 2.2 \times 10^4$ . These studies on 2D ribs are completed by numerical work such as the one of Panigrahi & Acharya, [14] who simulated a turbulent flow at  $Re = 1.4 \times 10^4$  on 2D square ribs. It shall be noted that none of the studies exposed in this bibliographic review presents cases with  $Re > 10^5$ , even if Castro & Robins [15] made the hypothesis that, for  $Re > 4000$ , the turbulent flow achieves a certain Reynold number independency. The results of the present study should provide complementary informations at higher Reynolds number in water on the flow past a 2D obstacle.

No study on inclined floor placed just downstream of a nominal 2D or 3D obstacle was found. The closest set up is the experimental study of dunes and the impact of the dune slope on the flow. However, the impact of an inclined floor on the wake of the obstacle as such is a different approach.

After presenting the experimental set-up, a spatial characterization of the wake past wide wall-mounted square obstacles is presented. A comparison with the cube case and the impact of the inclined floor addition are studied for low and high  $A_R$  cases. Then, a temporal analysis is presented and the velocity profiles that are created by various obstacle geometry are compared.

## II. EXPERIMENTAL SET-UP

### A. The tank and the obstacles

The tests are carried out in the wave and current circulating flume tank of IFREMER in Boulogne-sur-Mer presented in figure 2. The test section has the following dimensions: 18m length  $\times$  4m width  $\times$  2m height. The incoming flow is assumed to be steady and uniform. By means of grid

<sup>1</sup>2D obstacles are obstacles where a dimension is large enough to be considered infinite and a part of the flow can be considered as 2D

and honeycomb (that acts as a flow straightener) placed at the inlet of the working section (see fig. 3(a)), a turbulent intensity of  $I = 1.5\%$  (equation 1) is achieved. In this study, non dimensional lengths are used:  $x^* = x/H$ ,  $y^* = y/H$  and  $z^* = z/H$ , with  $H$  the obstacle height.

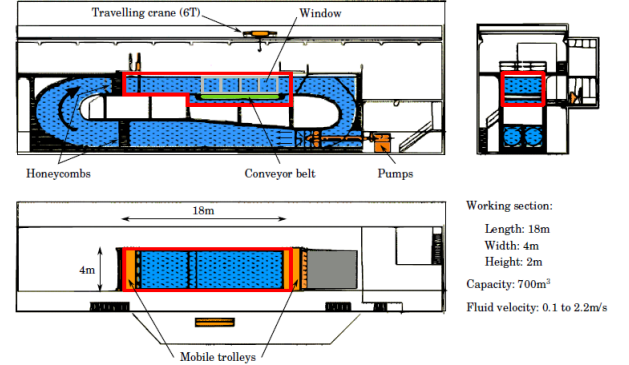


Fig. 2: IFREMER Flume tank in Boulogne-sur-Mer

In this work, we focus on the three instantaneous velocity components denoted  $(U, V, W)$  along the  $(X, Y, Z)$  directions respectively (Fig. 3(a)). The Reynolds decomposition is used allowing the decomposition of each instantaneous velocity component into a mean value and a fluctuation part:  $U = \bar{U} + u'$ , where an overbar indicates the time average. Turbulence intensity  $I$  in the incoming flow is defined as follows:

$$I = 100 \sqrt{\frac{\frac{1}{3}(\overline{u'^2} + \overline{v'^2} + \overline{w'^2})}{\bar{U}_\infty^2 + \bar{V}_\infty^2 + \bar{W}_\infty^2}} \quad (1)$$

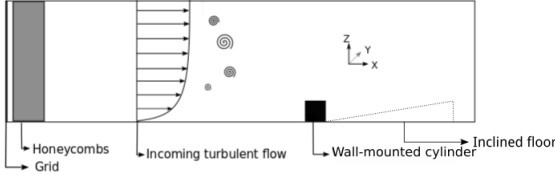
where  $(\bar{U}_\infty, \bar{V}_\infty, \bar{W}_\infty)$  are the uniform velocity components of the incoming flow. In the following, the denoted Reynolds shear stress component corresponds to  $\tau_{uw} = \overline{u'w'}$ .

	$U_\infty$ [m/s]	Rugosity height $H$ [m]	Depth $D$ [m]	$Re = \frac{H U_\infty}{\nu}$	$F_r = \frac{U_\infty}{\sqrt{gD}}$
Alderney Race	5	5	40	$2.5 \times 10^7$	0,25
Flume tank (1/20)	1	0,25	2	$2.5 \times 10^5$	0,23

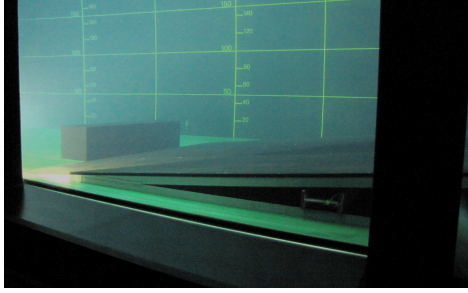
TABLE I: *in situ* and experimental conditions (1:20 scale)

All obstacles considered in this study are chosen to represent the real-life conditions at scale. Reynolds similitude could not be achieved so the experiments are carried out in a Froude similitude with a Reynolds number as high as achievable to be closer to real conditions. Each element represents a key bathymetric element in the area of interest at a 1:20 scale (see table I). The aspect ratio is defined as  $A_R = \text{width}/\text{height}$ . Previous experiments were achieved on a wall-mounted cube with height:  $H = 250 \text{ mm}$  ( $A_R = 1$ ) and results are detailed in [3,4]. For the present study, the first set of experiments

is carried out on wall-mounted cylinders with dimensions  $\text{length} \times \text{width} \times \text{height} = H \times 7H \times H$  ( $A_R = 7$ ). The experimental set-up consists in the same wall-mounted cylinders with an additional inclined floor downstream of the cube. The floor is a  $3m$  long  $\times$   $3m$  wide plane with an inclination of  $6.5^\circ$  representing a smooth variation of the bathymetry that exists at site: it represents an average elevation of 12 meters of the floor over 105 meters. The floor is disposed directly downstream of the cube. In the rest of this study, the obstacles will be referred to as  $C_n S_m$  with C for the wall-mounted obstacle and S for inclined floor,  $n$  is referring to the obstacle aspect ratio and  $m$  the floor inclination.



(a) Representation of the cube in the tank with (X,Y,Z) axis



(b) Picture of the cube in the tank with PIV shooting ( $C_1$  test case)

Fig. 3: Schematic view and picture of the cylinder and inclined floor in the wave and current circulating tank of IFREMER

### B. Measurement tools

To characterize the flow, 2D Laser Velocimetry techniques are used (see fig. 3(b)), the tank is seeded with  $10 \mu m$  diameter micro-particles. For the PIV (Particle Image Velocimetry) measurements, a Nd-YAG Laser GEMINI-LIKE is used with a Camera FLOWSENS EO-2M  $1600\text{pix} \times 1200\text{pix}$  that makes double images with a time step of  $1600 \mu s$  for case  $C_7$  and  $800 \mu s$  for case  $C_1$ . A particle is detected on 3 to 5 pixels. PIV acquisitions are made for  $150s$ , hence 2250 double images are taken with a  $15H_z$  acquisition frequency. The data are post processed with the software DYNAMIC STUDIO. The displacement of particles is calculated using a single pass Cross-Correlation on a  $32\text{pix} \times 32\text{pix}$  interrogation windows with 50% overlap [16]. Outliers are replaced with the Universal Outlier Detection [17]. Various cases are considered and summarized in the table II.

Obstacles	Plane spanwise position	number of planes	Pixel size [mm]	Plane size [mm]
$C_7$	$y^* = 0$	12	0.72	$1162 \times 581$
$C_1$	$y^* = 0$	10	0.23	$350 \times 275$

TABLE II: Precisions for PIV measurements.

The LDV (Laser Doppler Velocimetry) acquisitions are made using a 2D DANTEC FiberFLOW system. The probe is positioned both horizontally ( $(U, V)$  measurements) and vertically ( $(U, W)$  measurements) at various streamwise positions and along the Z or Y axis depending on the case. With LDV measurements, the acquisition frequencies are not constant, a re-sampling is done in the post processing. Based on previous works performed in the tank [18], we re-sample using the mean sample rate of the set of measurements considered.

Various sources of error can be identified. Positions fixed using the human eyes are considered to have an error of  $0.5 \text{ cm}$  and  $0.5^\circ$ ; it is the case for the obstacle and the lasers positioning. Particles motion follows the Basset-Boussinesq-Oseen equation; for silver-covered glass particle, the response of particle is of  $0.14 \text{ mm/s}$ . The laser sheet induces a magnification that causes an error of  $0.3\%$  [19]. Measurement standard deviation goes up to  $0.1\%$ . Calibration is achieved by the manufacturer for LDV. For PIV, calibration is precise to  $1 \text{ mm}$ . The pixel size is added to the errors for PIV measurements. Finally, vibration of the LDV probe can induce an error up to  $1 \text{ cm}$ . Hence, the errors on the results are of  $2\%$  and  $2.6\%$  for LDV and PIV respectively.

A comparison is made between the two measurement methods and on two obstacles with different aspect ratio ( $A_R = 6$  and  $A_R = 7$ ).  $\bar{U}$  profiles are plotted in figure 4 at various streamwise positions and in the plane of symmetry  $y^* = 0$  using the available database: LDV measurements for  $C_6$  and PIV measurements for  $C_7$ . Profiles at  $x^* = 1$  and  $x^* = 3$  are identical. For  $x^* > 5$ , a difference of about  $10\%$  to  $15\%$  appears for  $z^* < 2$ . This difference might be caused by the Velocimetry technique used, also note that this area is a highly turbulent zone where  $I \sim 20\%$ . Finally, it might be caused by the  $A_R$  difference, hence the side effect impact the case  $C_6$  sooner. However, considering the measurement errors present in that zone, two conclusions can be drawn from this comparison. First, the two measurement tools give similar results and some sameness of the  $C_6$  and  $C_7$  profiles. Second, these cases can be considered conjointly as a large  $A_R$  case  $C_L$  in the symmetry plane  $y^* = 0$ . It is confirmed by [7], that shows that for  $A_R > 6$ , the evolution of the wake with  $A_R$  is very smooth and that there is few difference between  $A_R = 6$  and  $A_R = 7$  ( $\sim 8\%$ ).

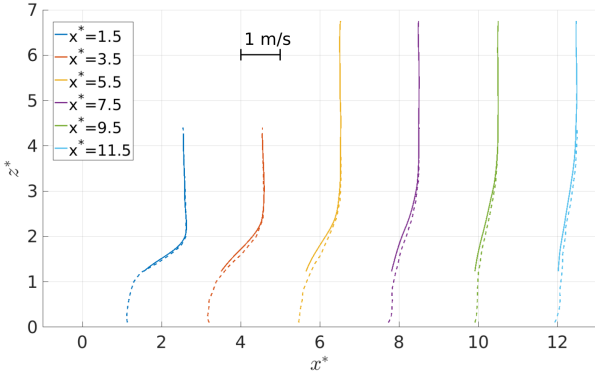


Fig. 4:  $\bar{U}$  profiles at positions  $x^* = 1.5, 3.5, 5.5, 7.5, 9.5, 11.5$  and  $y^* = 0$  for cases  $C_6$  (—) using LDV measurements and  $C_7$  (---) using PIV measurements.

### III. CHARACTERISATION OF THE WAKE PAST LARGE $A_R$ OBSTACLES

#### A. Large $A_R$ spatial characterisation

Streamlines are presented in figure 5. The recirculation length  $l^*$  is evaluated. We find:  $l^* = 6$ . In [7], for  $A_R = 7$ , they found  $l^* = 5.7$ , which is similar to our results, at a similar  $Re$ . In their study, the value of  $l^*$  then increases up to  $l^* = 8$  or 9 for ribs, which is closer to [10,11]. Furthermore, the flow shows an area of  $\bar{W} > 0$  at  $x^* = 6$  from the floor to  $z^* \sim 1$ . This causes the apparition of a stagnation point at  $x^* = 5, z^* = 1$ . Hence, due to the absence of side effects, the wake is impulsed towards the surface. Side effects then, tend to reduce the wake and redirect it towards the ground.

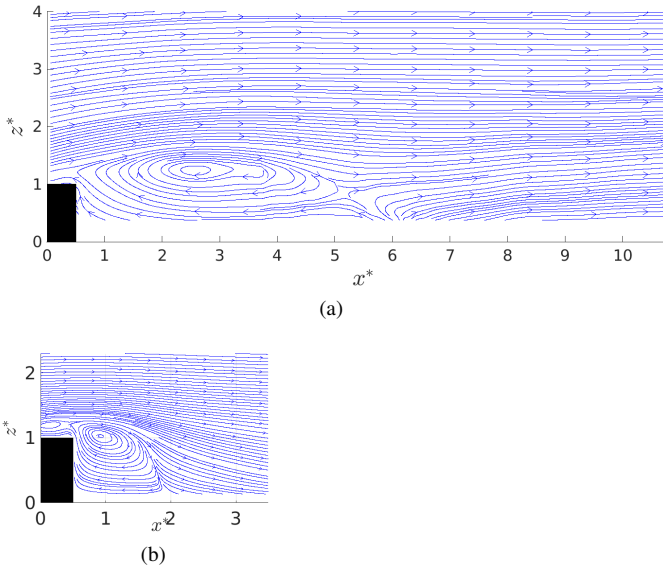


Fig. 5: Streamlines of case **a)**  $C_L$  and **b)**  $C_1$  from PIV measurements

Maps of averaged Reynolds shear stress  $\tau_{uw} = \overline{u'w'}$  are

presented in figure 6. When a fluid meets an obstacle, the flow separates between the outer steady region and the recirculation area where  $\bar{U} < 0$ . Between these two parts, the Reynolds shear stress is intense as can be seen on figure 6. This region is called shear layer; its form and intensity are an indication of the extend of the far wake of the obstacle. Even if some parts were badly lighted during measurements close to the floor, this figure shows the large shear region that appears to be directed towards the surface. It shall be remembered that the surface is at  $z^* = 8$ , hence the shear layer reaches half of the tank depth at  $x^* = 12$ . Furthermore, it is expected that structures are shed from the shear layer and rise near the tank surface. More precisions will be given in the chapter V.

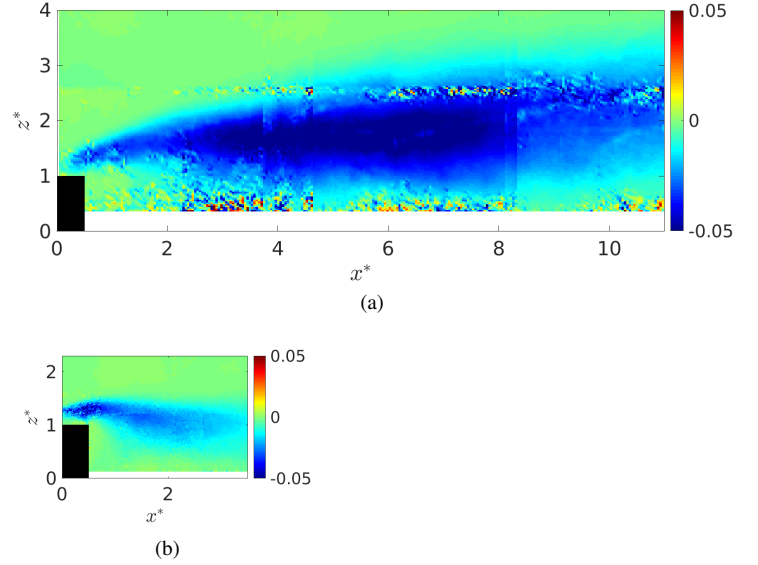


Fig. 6:  $\tau_{uw}$  of case **a)**  $C_L$  and **b)**  $C_1$  from PIV measurements

#### B. $A_R$ impact

The wall-mounted cube alone case was extensively studied in [3,4] and is here compared to case  $C_L$ , streamlines and Reynolds shear stress maps for case  $C_1$  are presented in figures 5(b) and 6(b). In figure 7, a schematic representation of the recirculation zone and wake of both cases in the plane  $y^* = 0$  is represented using  $\bar{U}$  maps. The recirculation lengths are  $l^*(C_1) = 1.9$  and  $l^*(C_L) = 6$ , hence for  $A_R$  that is six times superior, the recirculation triples due to the reduction of side effects in the symmetry plane  $y^* = 0$ . It is expected that the same occurs on the far wake, *i.e.* it triples, although no measurements were achieved that far.

Due to the increase of the aspect ratio, the side effects become less important in the middle plane. Additionally, the flow goes necessary over rather than around the obstacle. Both of these behaviour are causing the increase of the recirculation area and of the wake.



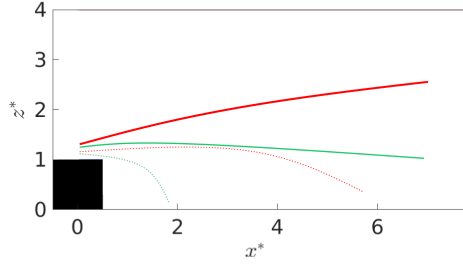


Fig. 7: Schematic representation of the recirculation (---), where  $\overline{U} < 0$  and the wake (—), where  $\overline{U} > 0.9$  for cases  $C_L$  (red) and  $C_1$  (green)

#### IV. EFFECT OF THE ADDITION OF AN INCLINED FLOOR ON THE CYLINDER WAKE

*In-Situ* conditions show various floor altitude variations. In order to represent smooth depth variations, an inclined floor is added downstream of the cubic wall-mounted obstacles. Its angle is  $\alpha = 6.5^\circ$  and is referred to as case  $S_6$ . The influence of the inclined floor on the cube is detailed in a previous paper [4]. Results showed the reduction of the circulation zone with the addition of the inclined floor. The shear layer was also reduced, thinner and reoriented towards the free surface. The effect of the inclined floor on the cylinder wake is investigated here.

Streamlines for cases  $C_L S_6$  are plotted in figure 8 and are to be compared to streamlines in figure 5. First obvious effect of the floor is the reduction of the recirculation length, we have  $l^*(C_L S_6) = 5.2$ , whereas  $l^*(C_L) = 6$ , hence a reduction of 13%. The comparison of the case  $C_1$  and case  $C_1 S_6$ , gave a reduction of  $l^*$  of 11% which is very similar to large aspect ratio case. The floor also seems to give a substantial impulsion to the cylinder wake towards the surface.

To evaluate the effect of the inclined floor on the flow development, the streamwise growth rate of the shear layer is estimated in the  $y^* = 0$  plane for both cases. First, the centre of the shear layer ( $z_0^*$ ) is determined for each streamwise position. It corresponds to the inflexion point of the mean velocity profile. Second, in each streamwise position  $x$ , the vorticity thickness is computed:

$$\delta_w(x) = \frac{U_s}{(dU_s/dz)_{z=z_0}} \quad (2)$$

where  $U_s = U_\infty - U_i(x)$  with  $U_i(x)$  the streamwise velocity underneath the shear layer.

In order to find the inflection point, for each streamwise position  $x$ , the streamwise velocity profile  $U_s(x, z)$  is fitted by a function  $f(x, z) = a(x) + b(x)\tanh(c(x)z)$ . Results are presented in figure 9 for both cases. Impact of the floor inclination is similar to case  $C_1$  [4]. The floor elevation causes the elevation and the thinning of the shear layer.  $z_0^*(C_L S_6)$  remains higher than  $z_0^*(C_L)$  and the difference

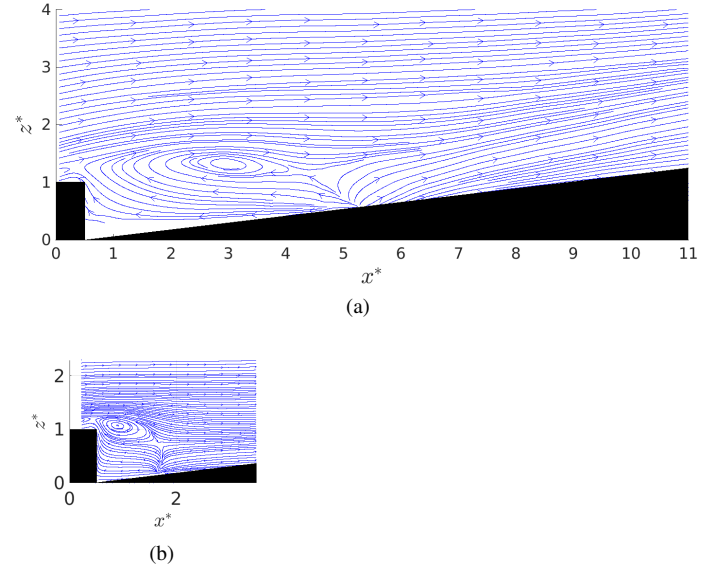


Fig. 8: Streamlines of case **a)**  $C_L S_6$  and **b)**  $C_1 S_6$  in the plane  $y^* = 0$  from PIV measurements.

between both increases from  $z_0^*(C_L S_6) - z_0^*(C_L) = 0.12$  at  $x^* = 3$  up to  $z_0^*(C_L S_6) - z_0^*(C_L) = 0.6$  at  $x^* = 8$ .  $\delta_w$  difference between both cases is very low  $\delta_w(C_L) - \delta_w(C_L S_6) = 0.01$  up to  $x^* = 6$  and then increases to reach  $\delta_w(C_L) - \delta_w(C_L S_6) = 0.13$  at  $x^* = 9$ . The floor position is indicated on figure 9(a) and it shows that the shear layer in case  $C_L S_6$  follows the floor elevation until  $x^* = 6$  and is then impulsed towards the surface. It shall be noted that  $x^* = 6$  is around the position of the reattachment of the recirculation zone.

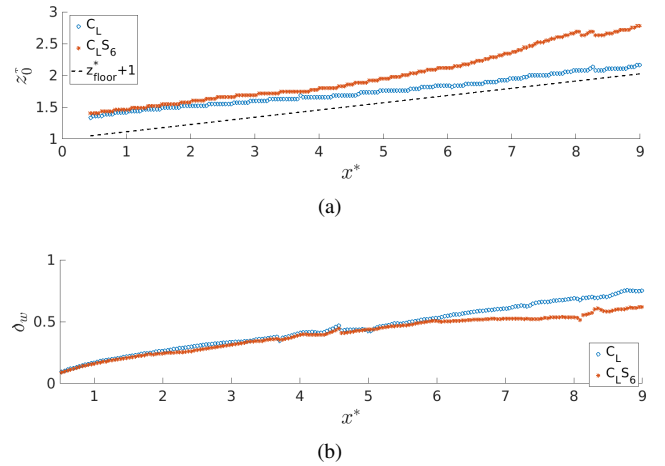


Fig. 9: **a)** Evolution of the shear layer centre altitude  $z_0^*$  with the inclination of the floor for comparison and **b)** streamwise evolution of the shear layer thickness  $\delta_w$  for case  $C_L$  using interpolated PIV measurements profiles.

To conclude, there are two zones on the wake past combina-

tion  $C_L S_6$ . For  $x^* < 6$  (before the recirculation ends), where the inclined floor does not have an impact: the wake develops the same way behind  $C_L$  and  $C_L S_6$  with only a translation given by the floor impulsion. Then, for  $x^* > 6$ , the inclined floor has a significant effect on the wake: the translation given by the floor triples and the shear layer becomes thinner.

## V. TEMPORAL ANALYSIS

With the LDV measurement system, the acquisition frequency allows a wider spectrum range and the acquisition time a good datarate. Samples have at least 20 000 points with an acquisition frequency between 15 and 300  $H_z$ . Fast Fourier Transform are used to plot Power Spectrum Densities (PSD) for the fluctuating velocity component.

### A. Large $A_R$ temporal characterisation

Points where the temporal analysis is performed are presented in figure 10, their positions are: A(5.5; 0; 4), B(15.5; 0; 6), C(3.5; 0; 3.6), D(3.5; -1; 3.6) and E(3.5; -2; 3.6). Points C, D and E allow a spanwise comparison to understand the impact of side effects. A is a point higher and further away to understand the evolution of the wake and point B is one of the point with most distance to the obstacle achievable in the tank.

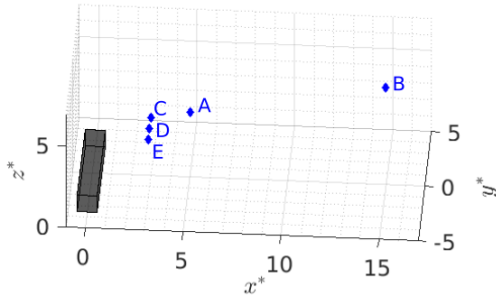


Fig. 10: Positions of A B C D E for PSD spectrum study of LDV measurements.

Cases  $C_L$  and  $C_L S_6$  are compared with the  $u'$  component spectrum in figure 11, PSD are plotted versus the Strouhal number defined as  $S_t = fH/U_\infty$ . A peak appears on the spectrum of both cases and for positions A and B on the  $u'$  component. When the flow meets an obstacle, a shear layer is generated and vortex are shed from the shear layer into the flow at a precise frequency which corresponds to the shedding frequency that will be referred to as  $S_t^p$ . A slight difference of the peak is visible between both cases:  $S_t^p(C_L) = 0.065$  and  $S_t^p(C_L S_6) = 0.074$ . In the literature [20,21], another non-dimensional frequency can be found using the recirculation length  $l$  that is different with or without the inclined floor. If we consider  $S_{tl} = fl/U_\infty$ , we have  $S_{tl}^p(C_L) = S_{tl}^p(C_L S_6) = 0.39$ . Hence, the inclined floor has an impact on the recirculation length but not on the turbulent organisation of the shear layer and the structures being shed. The floor elevation impact appears to be on the

near wake and not so much in the far wake.

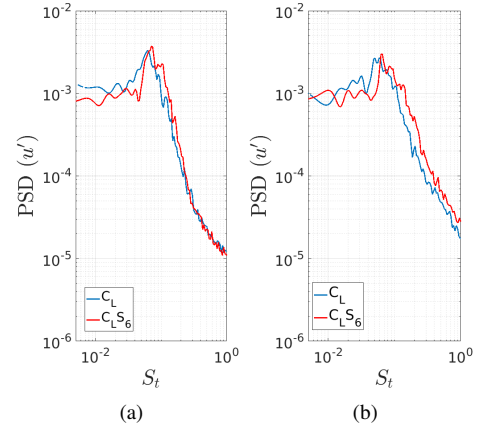


Fig. 11: PSD( $u'$ ) for cases  $C_L$  (blue) and  $C_L S_6$  (red) at a) A and b) B.

Figure 12 shows the PSD for all velocity components at point A. The shedding peak appears on PSD( $u'$ ) and PSD( $w'$ ) but not on PSD( $v'$ ). The vortex detected here is then in the  $(x, z)$  plane. The 3D effects caused by side effects do not affect the wake in the plane  $y^* = 0$ .

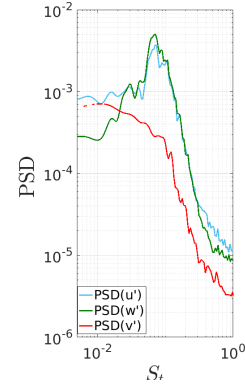


Fig. 12: PSD( $u'$ ) (blue), PSD( $v'$ ) (red) and PSD( $w'$ ) (green) for case  $C_L S_6$  in A.

The shedding peak evolution along the  $Y$  axis is studied in figure 13. It shows that a peak appears for  $y^* < 0$  on  $v'$  and that the peak on  $u'$  is still present but less intense. Hence, vortices in the plane  $(x, y)$  are detected and side effects appears as soon as  $y^* \geq 1$ . These vortices are generated by the vertical sides of the wall-mounted cylinder.

The furthest position downstream of the obstacle where LDV measurements are performed is  $x^* = 19.5$  and  $z^* = 6$ . At this point, the peak is still visible (PSD are not presented here). It is remembered that the free surface is at  $z^* = 8$ . Hence, this point is close to the surface. It is then expected that perturbations might reach the free surface.

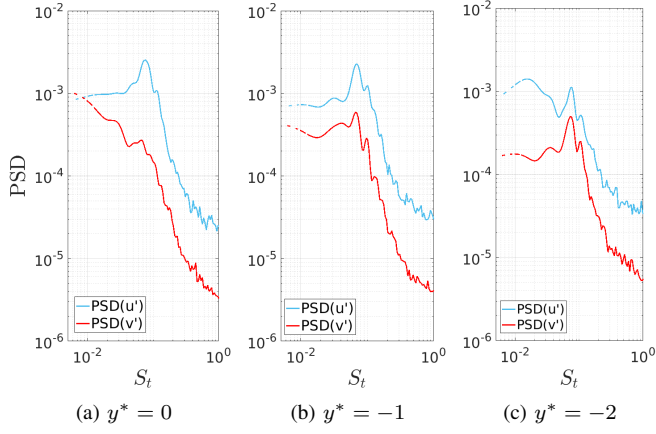


Fig. 13: PSD( $u'$ ) (blue) and PSD( $v'$ ) (red) for case  $C_L S_6$  in **a) C**, **b) D** and **c) E**.

### B. $A_R$ impact

The same temporal analysis is achieved on case  $C_1$  for two points at different spanwise positions using LDV measurements. Results for all velocity components are presented in figure 14. First observation is the shedding frequency peak that shifts to  $S_t^p = 0.09$  (superior to  $C_L$ ). In the symmetry plane  $y^* = 0$ , the peak appears on  $v'$  only. But, for  $y^* = 0.5$ , it appears on all components. The presence of a peak on  $v'$  in  $y^* = 0$  should be a mark of  $(x, y)$  vortices, however no peak appears on  $u'$ . As explained by McArthur et al. [22] who studied the wake past Ahmed bodies, the shedding peak is proportional to the fluctuating velocity intensity. In the plane  $y^* = 0$ ,  $\tau_{uu} = 0$  and then its value rises for  $y^* \neq 0$  whereas  $\tau_{vv}$  presents a peak at  $y^* = 0$  and decreases for  $y^* \neq 0$ . This causes an absence of  $u'$  peak at  $y^* = 0$  and the reduction of the  $v'$  peak intensity at  $y^* \neq 0$ . Vortices hereby detected are in the  $(x, z)$  plane, this is caused by the side effects. Indeed, this peak was absent for case  $C_L$ . The absence of  $w'$  peak might be caused by the symmetry as well.

It shall be noted that the shedding peak is obtained at a higher  $S_t$  for case  $C_1$  indicating more frequent structures. Additionally, fluctuating velocity maps are plotted in figure 15. For case  $C_1$ , as mentioned in chapter II, PIV planes are smaller than for case  $C_L$ . For each case, one of the more intense turbulent event is represented. It is obvious on the maps that events are much larger for case  $C_L$  than for case  $C_1$ . Also, as expected, these structures reach further and higher positions for large  $A_R$ : the vortex centre is at  $x^* = 14.7$ ,  $z^* = 4$  for  $C_L$  and  $x^* = 2.5$ ,  $z^* = 1.5$  for  $C_1$ .

Conclusion is that, turbulent events are more frequent for smaller aspect ratio case  $C_1$  and they are much smaller and less intense compared to case  $C_L$ .

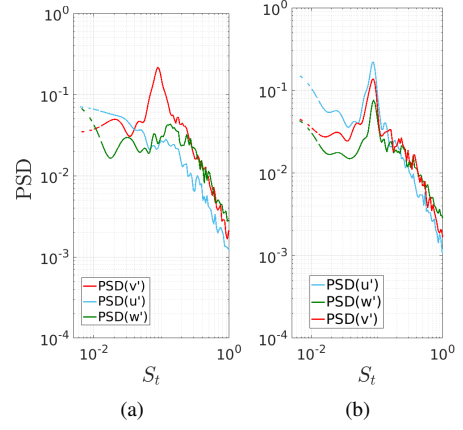


Fig. 14: PSD( $u'$ ) (blue), PSD( $v'$ ) (red) and PSD( $w'$ ) (green) for case  $C_1$  in  $x^* = 2$ ,  $z^* = 0.7$  **a)  $y^* = 0$**  and **b)  $y^* = 0.5$** .

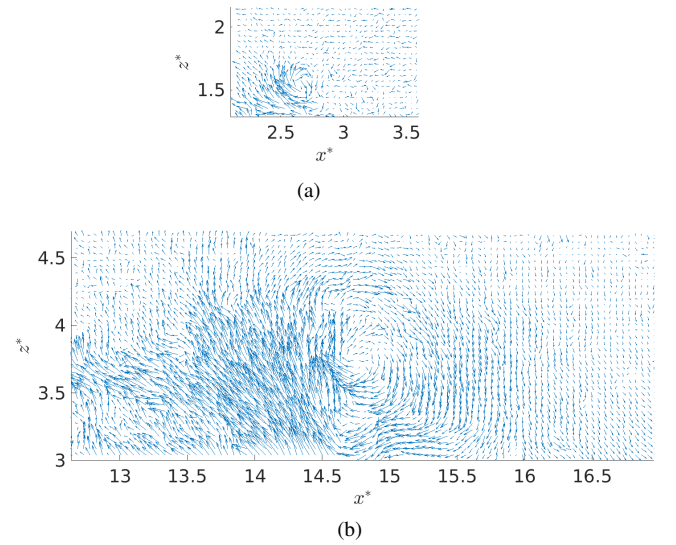


Fig. 15: Fluctuating velocity field for **a) case  $C_1$ , small PIV plane** and **b) case  $C_7$ , large PIV plane**.

## VI. IMPACT OF THE OBSTACLE GEOMETRY ON THE VELOCITY PROFILES

### A. Averaged velocity profiles

Turbines are meant to be installed in the Alderney race and, the final goal of the present study is to predict the velocity profiles impacting the turbine. In reality, turbines have a diameter of 15 m and are positioned on the seabed with the hub at a 20 m altitude. In the tank, at a 1/20 scale, it would mean at mid-depth, so between  $z^* = 2.6$  et  $z^* = 5.4$ . Two cases are considered: low  $A_R$  ratio case  $C_1$  and high aspect ratio case  $C_L$ . For the first case, we consider the near wake ( $x^* = 1$ ) and far wake ( $x^* = 3$ ) and for the second case, the near ( $x^* = 5$ ), middle ( $x^* = 11$ ) and far wake ( $x^* = 19$ ). Using PIV and LDV measurements, we are able to get profiles for  $z^* \in [2.5; 4]$ .

In order to understand the different impact of the geometries in  $z^* \in [2.5; 4]$ , a schematic representation inspired from figure 7 for both cases is made in figure 16. For case  $C_1$ , perturbations do not reach the altitude on interest here. Hence, no profiles are plotted for that case. However, for case  $C_L$ , the wake does have a strong impact from  $x^* \geq 6$ .

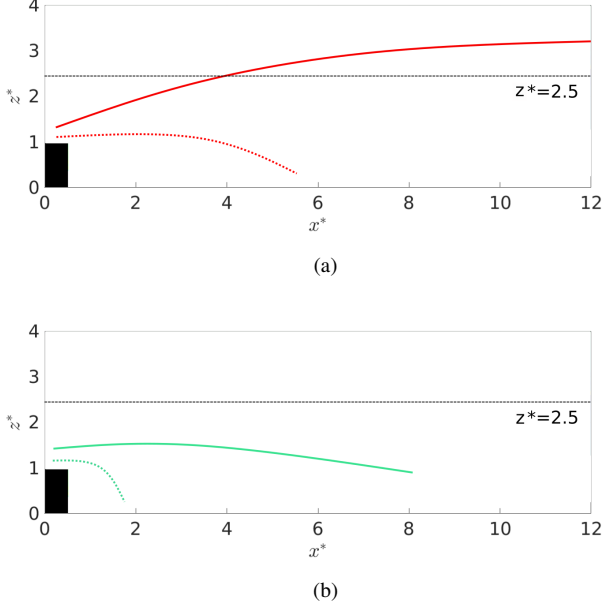


Fig. 16: Schematic representation of the recirculation (---), where  $\bar{U} < 0$  and the wake (—), where  $\bar{U} > 0.9$  for cases **a)**  $C_L$  (red) and **b)**  $C_1$  (green). Black dots indicate  $z^* = 2.5$  in horizontal.

In order to evaluate the impact of  $C_L$  on the velocity profiles at the turbine altitude,  $\bar{U}$  are plotted for  $x^* \in [0.5; 11.5]$  from LDV measurements in figure 17(a) and at  $x^* \in [13; 19]$  from PIV measurements and in figure 17(b) for  $z^* > 2.5$  since measurements are not available at a lower altitude. In the shear layer, for  $x^* = 5.5$ ,  $z^* = 1.4$ ,  $u_{rms} = 34\%$ , and, at the turbines altitude ( $x^* = 9.5$ ,  $z^* = 2.8$ ),  $u_{rms} = 20\%$ , it is lower but remains elevated compared to the value in the outer flow. This value remains identical until  $x^* = 13$ ,  $z^* = 2.8$  and then starts decreasing for  $x^* = 19$ ,  $z^* = 4$ , where  $u_{rms} = 14\%$ . The profiles show the increase of turbulence intensity above  $z^* = 2.5$ . Near the obstacle, turbines should not be impacted by the obstacle, however for  $x^* > 5$ , turbulent structures might have a strong impact on the turbines.

Temporal series of  $u'$  are plotted in figure 18 for cases  $C_1$  and  $C_L$  at a fixed point. This figure illustrates the extend of the wake past wide  $A_R$  objects compared to small  $A_R$  objects. In average,  $\bar{u}'$  is 10 times higher for  $C_L$ . This can be understood looking at figure 7 that shows that the chosen point is in the wake of  $C_L$  but not  $C_1$ . At this point, the PSD have a very different intensity, proportional to  $u'$ . The shedding peak is detected for both cases, although, as explained in chapter V,

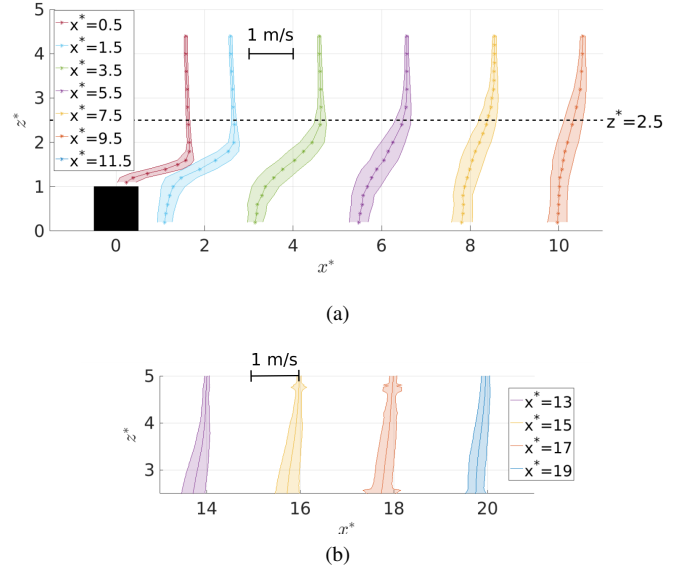


Fig. 17:  $\bar{U}$  profiles with  $u_{rms} = \sqrt{u'u'}$  for case  $C_L$  at **a)**  $x^* = 0.5; .5; 3.5; 5.5; 7.5; 9.5; 11.5$  from LDV measurements and **b)** at  $x^* = 13; 15; 17; 19$  from PIV measurements

the frequency of emission of shed vortices is higher for  $C_1$  than for  $C_L$ .

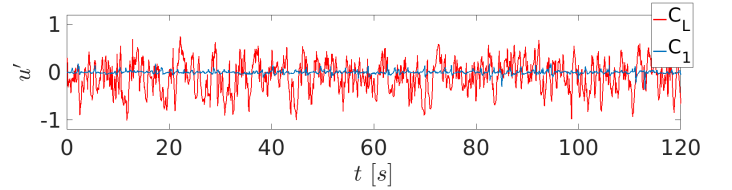


Fig. 18: Temporal series of  $u'$  for cases  $C_1$  (blue) and  $C_L$  (red) at point  $(x^* = 3.5, y^* = 0; z^* = 1.6)$  over 120 s. Data from LDV measurements.

### B. Turbulent structures impact

In chapter V, using LDV measurements a spectral peak for case  $C_L$  is detected for  $S_t^p = 0.65$ , or  $f^p = 0.26 H_z$  hence 39 vortices detected for 150 s. In figure 19, a map of instantaneous  $u'w'$  for  $z^*$  versus  $t$  is plotted for a chosen streamwise position  $x^*$ . A vortex passing is detected [23] with a high  $u'w' > 0$  peak followed by  $u'w' < 0$  with amplitude  $> 0.02$ . At mid-height  $z^* = 3.7$ , we count  $\sim 40$  vortices in 150 s of PIV acquisition. This matches the number found with LDV measurements. Another aspect is the fact that some events are more energetic than others and are still persistent above  $z^* = 4.5$ . These highly turbulent events that rise higher than others can have a strong impact on the turbine structure and production.

## VII. CONCLUSION AND PERSPECTIVES

In the present paper, the wake past wall-mounted cubic elements with two aspect ratios is investigated. PIV and



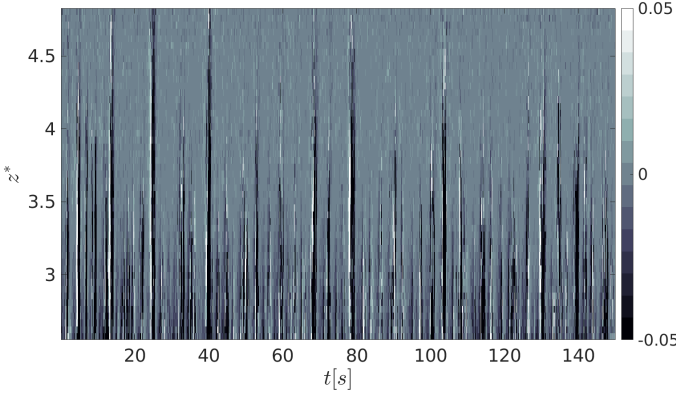


Fig. 19:  $u'w'$  in a  $z^*$  versus  $t$  map at  $x^* = 10.8$  for case  $C_L$ . From PIV measurement

LDV measurements are used and experimental conditions are chosen to be representative of real-life conditions in the Alderney Race.

First, spatial analysis is performed using PIV measurements. The wake past large aspect ratio cylinder  $C_L$  is studied. A comparison is then made between  $C_1$ , the wall-mounted cube and  $C_L$ , the wall-mounted cylinder. It appears that for  $A_R$  that is six times superior, the recirculation area triples due to the reduction of side effects on the cylinder. Afterwards, the study of the impact of the floor inclination on the wake is made. It is found that the inclined floor causes a reduction of 13% of the recirculation length, which is similar to the cube case. The thickness and centre position of the shear layer are studied and conclusion is that the inclined floor redirects the shear layer towards the surface. The shear layer becomes thinner with the inclination of the floor. The inclined floor has a similar impact on the wake of a 3D wall-mounted cube [4].

Then, a temporal study is performed using LDV measurements. A shedding peak is detected on the spectrum. For case  $C_L S_6$ , this peak appears only on  $u'$  and  $w'$  in the middle plane ( $y^* = 0$ ), when getting closer to the edges of the cylinder ( $y^* \neq 0$ ), a peak on  $v'$  appears with the apparition of side effects. In case  $C_1$ , however, the 3D wake is more complex and only  $v'$  shows a peak in the plane  $y^* = 0$  and all three components on the plane  $y^* = 0.5$ . Hence, the structures shed into the flow are very different for large and small  $A_R$  obstacles. For case  $C_1$ , turbulent structures are small in size, frequent and they do not reach higher altitudes. Whereas, for case  $C_L$ , they are much larger, they appear less frequently and can be seen much higher and further from the obstacle in the flow.

Finally, the turbulent velocity profiles for different bottom geometries are studied. As expected, the larger the aspect ratio, the higher the turbulence intensity at the position where turbines are meant to be installed. Depending on the distance

to the obstacle, velocity profiles show low or high turbulence intensity. Furthermore, strong turbulent events, additionally to the vortex shed from the shear layer are detected. All of these turbulent events might cause a strong load on the turbine and will have to be characterised through additional PIV and LDV measurements. The size, trajectory and intensity of such structures is an essential part of the understanding of turbulence in the Alderney Race.

The present study is placed in a larger project called THYMOTÉ (with France Énergies Marines). It includes numerical work and *in-situ* measurements. This work is also meant to create a database for numerical work ([24]–[26]). Their aim is the modelization of turbulence in the Alderney Race, the obstacles tested in the tank are usable for numerical benchmark.

#### ACKNOWLEDGEMENT

This work benefits from a French State grant managed by the National Research Agency under the Investments for the Future program bearing the reference ANR-10-IEED-0006-11. The authors also acknowledge the financial support of IFREMER and the Hauts de France Regional Council for this PhD study. We are most grateful to Thomas Bacchetti and Jean-Valéry Facq for their assistance and precious advices.

#### REFERENCES

- [1] O. Durán Medina, F. Schmitt, R. Calif, G. Germain, and B. Gaurier, “Turbulence analysis and multiscale correlations between synchronized flow velocity and marine turbine power production,” *Renew. Energ.*, vol. 112, pp. 314–327, 2017.
- [2] P. Mycek, B. Gaurier, G. Germain, G. Pinon, and E. Rivolaen, “Experimental study of the turbulence intensity effects on marine current turbines behaviour. part I: One single turbine,” *Renew. Energ.*, vol. 66, pp. 729–746, 2014.
- [3] M. Ikhennecheu, P. Druault, B. Gaurier, and G. Germain, “An experimental study of influence of bathymetry on turbulence at a tidal stream site,” *EWTEC*, 2017.
- [4] M. Ikhennecheu, B. Gaurier, P. Druault, and G. Germain, “Experimental analysis of the floor inclination effect on the turbulent wake developing behind a wall mounted cube,” *In revision*, 2018.
- [5] W. Schofield and E. Logan, “Turbulent shear flow over surface mounted obstacles,” *J. Fluid Eng.*, vol. 112, pp. 376–385, 1990.
- [6] Y. Lee, S. Boo, H. Lim, and K. Misutani, “Pressure distribution on rectangular buildings with changes in aspect ratio and wind direction,” *Wind Struct.*, vol. 23, pp. 465–483, 2016.
- [7] R. Martinuzzi and C. Tropea, “The flow around surface-mounted, prismatic obstacles placed in a fully developed channel flow, (*Data Bank Contribution*),” *J. Fluid Eng.*, vol. 115, pp. 85–92, 1993.
- [8] J. Chou and S. Chao, “Branching of a horseshoe vortex around surface-mounted rectangular cylinders,” *Exp. Fluids*, vol. 28, pp. 394–402, 2000.
- [9] I. Castro, “Relaxing wakes behind surface-mounted obstacles in rough wall boundary layers,” *J. Fluid. Mech.*, vol. 93, pp. 631–659, 1979.
- [10] Y. Liu, F. Ke, and H. Sung, “Unsteady separated and reattaching turbulent flow over a two-dimensional square rib,” *J. Fluid Struct.*, vol. 24, pp. 366–381, 2008.
- [11] G. Bergeles and N. Athanassiadis, “The flow past a surface-mounted obstacle,” *J. Fluid Eng.*, vol. 105, pp. 461–463, 1983.
- [12] R. J. Hearst, G. Gomit, and B. Ganapathisubramani, “Effect of turbulence on the wake of a wall-mounted cube,” *J. Fluid Mech.*, vol. 804, pp. 513–530, 2016.
- [13] L. Wang, M. Salewski, and B. Sundén, “Turbulent flow in a ribbed channel: Flow structures in the vicinity of a rib,” *Exp. Therm. Fluid Sci.*, vol. 34(2), pp. 165–176, 2009.

- [14] P. Panigrahi and S. Acharya, "Multi-modal forcing of the separated shear flow past a rib," *J. Fluid Eng.*, vol. 126, pp. 22–31, 2004.
- [15] I. Castro and A. Robins, "The flow around a surface-mounted cube in uniform and turbulent streams," *J. Fluid Mech.*, vol. 79, pp. 307–335, 1977.
- [16] C. Meinhart, A. Prasad, and R. Adrian, "A parallel digital processor system for particle image velocimetry," *Meas. Sci. Technol.*, vol. 4, pp. 619–626, 1993.
- [17] J. Westerweel and F. Scarano, "Universal outlier detection for PIV data," *Exp. Fluids*, vol. 39, pp. 1096–1100, 2005.
- [18] O. Durán Medina, F. Schmitt, R. Calif, G. Germain, and B. Gaurier, "Correlation between synchronised power and flow measurements, a way to characterize turbulent effects on a marine current turbine," *EWTEC*, 2015.
- [19] R. Adrian and J. Westerweel, "Particle image velocimetry," *Cambridge University Press, Cambridge*, 2011.
- [20] N. Cherry, R. Hillier, and M. Latour, "Unsteady measurements in a separated and reattaching flow," *J. Fluid Mech.*, vol. 144, pp. 13–46, 1984.
- [21] K. Sarkar and B. Mazmunder, "Turbulent flow over the trough region formed by a pair of forward-facing bedform shapes," *European J. of Mechanics B/Fluids*, vol. 46, pp. 126–143, 2014.
- [22] D. McArthur, D. Burton, M. Thompson, and J. Sheridan, "On the near wake of a simplified heavy vehicle," *J. Fluid. Struct.*, vol. 66, pp. 293–314, 2016.
- [23] J. Wallace, "Quadrant analysis in turbulence research: history and evolution," *Annu. Rev. Fluid Mech.*, vol. 48, pp. 131–158, 2016.
- [24] M. Mercier, M. Grondeau, d. T. J. Guillou, S. a, and E. Poizot, "Towards the modelling of turbulence at tidal stream power sites with the lattice boltzmann method," *EWTEC*, 2017.
- [25] A. Bourgoin, S. Guillou, J. Thiébot, R. Ata, and S. Benhamadouche, "Development of a large-scale eddy simulation approach for tidal currents modelling," *EWTEC*, 2017.
- [26] A. Bourgoin, S. Guillou, R. Ata, J. Thiébot, and S. Benhamadouche, "Tidal current characterization with large eddy simulation," *AWTEC*, 2018.